STU SLOVAK UNIVERSITY OF TECHNOLOGY IN BRATISLAVA

Journal of Electrical Engineering, Vol. 77, No. 2, 2026, pp. 148-161
https://reference-global.com/journal/JEE

Isolation enhancement in dual-polarized patch antennas using TM_{21} and TE_{20} modes for 6G sub-THz transceiver applications

Shanmugasundaram Bhoopalan[1], Umathurai Saravanakumar[1], Jayaraman Kirubakaran[1], Muddineni Raveendra[2]

This study focuses on enhancing isolation in dual polarization antennas operating at different modes in order to suppress coupling between transmitter (Tx) and receiver (Rx) without using any additional decoupling modelling. To validate the proposed investigation approach, a transmitter antenna was simulated at 150 GHz in vertical polarization (V-Pol), and the Rx works at 180 GHz in horizontal polarization (H-Pol). Later, both Tx and Rx were coupled in such a way that they excite in orthogonal directions to each other, implying that the angle between Tx and Rx is approximately 90 degrees. In this case, the Tx will function in TM_{21} resonance mode, having an operational bandwidth of 10 GHz at 150 GHz. While Rx will operate in TE_{20} mode, with an operational bandwidth of more than 10 GHz at 180 GHz. This research achieves more than 30 dB isolation simply by allowing Tx and Rx to operate in different modes under an orthogonal feeding setup. The proposed antenna provides better than $|S_{12}| > 30$ dB isolation with an isolation bandwidth of 51.42% in the sub-THz range from 130 GHz to 220 GHz without the need for an extra decoupling mechanism. Finally, the results of the proposed research were validated using HFSS and FEKO electromagnetic tools to explain simulation outcomes such as return loss, isolation, radiation efficiency, peak gain, and radiation patterns.

Keywords: isolation enhancement, dual polarization, mode characteristics, isolation bandwidth, 6G, sub THz transceiver applications

1 Introduction

With the global push for sixth-generation (6G) wireless technology gathering traction, researchers and engineers are venturing into new territory in communication systems. A crucial step ahead in this evolution is the transition from millimeter-wave frequencies, which serve as the foundation for 5G networks, to the higher terahertz frequency range envisaged for 6G. This transformation has the potential to provide extremely high data rates and minimal latency, but it also introduces complex challenges, particularly in antenna design and system integration. Fifth-generation (5G) networks, which operate at mmWave frequencies spanning from 30 to 300 GHz, can handle gigabit-per-second data rates and have enabled new applications such as augmented reality and self-driving automobiles. Looking ahead, the wireless communication industry is turning its focus to the THz spectrum (100 GHz to 10 THz) to meet 6G's stringent performance requirements, which include data rates approaching 1 Tbps (terabit per second) and sub-millisecond latency [1]. The substantially higher bandwidths accessible in the THz range make it ideal for data-intensive applications such immersive extended reality (XR), brain-computer interfaces, and holographic communication [2]. Despite the potential capabilities of THz frequencies, designing and implementing efficient THz antennas presents numerous significant hurdles. One important difficulty is free-space route loss and air absorption, which significantly limits the propagation distances and necessitate high-gain, directional antennas. Furthermore, antenna downsizing at these high frequencies needs remarkable fabrication precision, as even minor geometric errors can result in significant performance degradation [2]. In 6G sub-terahertz frequency bands, the requirement for high isolation between transmit (Tx) and receive (Rx) antennas becomes increasingly stringent, particularly for frequency division duplex (FDD) transceiver architectures, where simultaneous transmission and reception occur over adjacent frequency bands. Unlike lower microwave or millimeter-wave systems, sub-THz operation introduces severe electromagnetic challenges due to extremely compact electrical dimensions, enhanced surface-wave propagation, and strong near-field coupling between closely integrated antenna elements. As a result, even minor structural asymmetries or substrate interaction can lead to substantial leakage of transmitted power into the receive path. From a system perspective, insufficient Tx-Rx isolation

6

[1] Department of Electronics and Communication Engineering, Muthayammal Engineering college, Rasipuram, India
[2] Department of Electronic Engineering, National Ilan University, Yilan City, Taiwan
bhoopalanjp@gmail.com, saran.usk@gmail.com, kirubakaranj.rnd@gmail.com, muddineniravi962@gmail.com

https://doi.org/10.2478/jee-2026-0016, Print (till 2015) ISSN 1335-3632, On-line ISSN 1339-309X

directly impacts receiver linearity and sensitivity, as high-power leakage from the transmitter can saturate low-noise amplifiers, increase the effective noise floor, and introduce intermodulation products through nonlinear components. These effects are particularly detrimental in sub-THz links, where propagation losses are already significant and link margins are inherently limited. Consequently, achieving adequate isolation is not merely a matter of electromagnetic compatibility, but a fundamental requirement for maintaining dynamic range, error-vector magnitude (EVM), and overall link reliability in 6G communication systems. Furthermore, traditional isolation enhancement techniques commonly employed at lower frequencies – such as RF circulators, ferrite isolators, absorptive shielding, or discrete de-coupling networks – become increasingly impractical at sub-THz frequencies.

In this context, antenna-level self-isolation emerges as a highly effective and scalable solution for FDD-based sub-THz systems. By exploiting orthogonal polarizations, spatial mode diversity, or distinct electromagnetic modes, Tx and Rx antennas can be inherently decoupled without relying on additional lossy or bulky components. Such intrinsic isolation mechanisms suppress mutual coupling at the source, thereby reducing system complexity while preserving radiation performance [11]. Mode-based isolation strategies are particularly attractive at sub-THz frequencies, where higher-order modes can be selectively excited to achieve strong field orthogonality and radiation nulls between co-located antennas. Moreover, high self-isolation at the antenna level enables simultaneous and continuous bidirectional operation, which is essential for FDD systems targeting ultra-low latency and high spectral efficiency. As 6G networks are expected to support applications such as holographic communications, high-resolution sensing, and ultra-reliable low-latency links, the ability to maintain stable Tx-Rx coexistence becomes a decisive factor in transceiver design [12], [13]. Therefore, self-isolated antenna configurations not only enhance electromagnetic performance but also facilitate compact integration, reduced power consumption, and improved system robustness. the necessity of achieving high Tx-Rx self-isolation in sub-THz 6G FDD systems is driven by a combination of electromagnetic, circuit-level, and system-level constraints. Antenna designs that inherently suppress mutual coupling through polarization or mode orthogonality provide an efficient and practical pathway to overcoming these challenges, making self-isolation a key enabling technology for next-generation sub-THz wireless transceivers [14, 15].

Most of the existing works rely on additional structural or material-based de-coupling techniques, such as mutual coupling reduction (MCR), graphene-based coatings, cross stubs, or defected ground structures (DGS), to achieve acceptable isolation levels. While these approaches are effective to a certain extent, they often introduce design complexity, increased footprint, or performance trade-offs in terms of bandwidth and efficiency. For instance, the antenna reported in [3] operates at 28 GHz using an MCR-based decoupling mechanism and achieves an isolation of 25 dB with a moderate impedance bandwidth of 42.85%. However, the efficiency and peak gain remain limited due to additional resonant loading introduced by the decoupling structure. Similarly, the graphene metal coating approach in [4] provides improved isolation of 30 dB but suffers from a narrow bandwidth (19.17%) and lacks reported efficiency and gain data, making its overall radiation performance difficult to assess. Designs employing cross stubs [5] and DGS techniques [6-8] demonstrate that higher isolation can be achieved at lower or mmWave frequencies. However, these benefits come at the cost of increased antenna size, reduced bandwidth, or degraded radiation efficiency. In particular, the DGS based antennas exhibit either extremely narrow bandwidths (as low as 1.5% in [6]) or relatively low isolation levels (15 dB in [8]), indicating a clear trade-off between decoupling strength and impedance bandwidth. Moreover, the incorporation of ground-plane perturbations can adversely affect radiation stability and complicate fabrication, especially for higher-frequency applications [9, 10].

In contrast to the above-mentioned designs, the proposed antenna achieves high isolation through an intrinsic electromagnetic mechanism rather than by introducing external decoupling structures. The enhanced isolation originates from the deliberate excitation of orthogonal resonant modes in the transmitter and receiver elements, combined with an orthogonal feeding configuration. Specifically, the Tx operates in the TM_{21} mode under vertical polarization, while the Rx excites the TE_{20} mode under horizontal polarization, resulting in inherently weak field overlap between the two ports. Since the dominant surface current distributions and radiated fields are oriented in mutually orthogonal directions, the coupling paths between the Tx and Rx are effectively suppressed at the modal level. As a result, an isolation exceeding 30 dB is achieved across a wide isolation bandwidth of 51.42% in the sub-THz range, despite the absence of any dedicated decoupling element. Furthermore, the avoidance of additional decoupling structures eliminates parasitic loading and ground perturbations commonly observed in prior works, thereby preserving radiation efficiency and impedance bandwidth. This modal-orthogonality-based approach enables the proposed antenna to simultaneously realize wide bandwidth, high isolation, and near-unity efficiency within a compact footprint, clearly distinguishing it from previously reported designs that rely on structural or material-based decoupling techniques. Overall, the comparison clearly demonstrates that the proposed antenna effectively overcomes the common limitations observed in existing designs by simultaneously achieving wide bandwidth, high isolation, and near-unity efficiency in a compact form factor, without relying on conventional decoupling techniques. This highlights the robustness and scalability of the proposed approach, making it particularly suitable for next-generation sub-THz and beyond 5G and 6G wireless systems.

In this section, we covered the introduction to the proposed antenna for sub-THz 6G applications. Section 2 describes the proposed antenna's design and functionning concept, as well as its modelling. Section 3 will describe the suggested antenna's sensitive performance investigation using parametric analysis. In the same section, the isolation augmentation will be discussed. Later, the radiation efficiency, peak gain, and radiation patterns of the suggested antennas Tx and Rx will be discussed in depth, along with a comparison of literature antennas for completeness. Section 4 includes the conclusion.

2 Proposed antenna design

To design the proposed dual polarization antenna as shown in Figs. 1(a) and (b), initially the Tx has been designed at TM_{21} resonance mode at 150 GHz in V-Pol. To design Tx, initially, a ground copper line was designed with width $q = 0.1$ mm and length $p = 2$ mm which is exactly one λ at the target resonance frequency of Tx that is 150 GHz. Later, to design the substrate for the proposed antenna, the various PCB materials have been studied in [9, 10]. The authors used Teflon substrate with dielectric constant 2.2 and loss tangent 0.002 and they also fabricated their proposed antenna to confirm their simulation results with practical results. Therefore, in our research we choose the same electrical specification to design the substrate with length and widths are equal to $\lambda\times\lambda$ at 150 GHz (λ is the wavelength of the electromagnetic wave in the free space). In this situation the thickness of the Teflon substrate is approximately 10 mils (0.254 mm). Later a rectangular patch has been mounted on the Teflon substrate. The rectangular slots length and widths were also the same as the substrate design. The thickness of the rectangular patch is 10 μm. Then a circular slot has been integrated over the rectangular patch. The slot thickness is also same as rectangular patch thickness. In this case the radius of the circular slot is about 0.8 mm. As mentioned before, the Tx will be resonated at TM_{21} mode in V-Pol and its resonance frequency will be calculated from Eqn. (1), where $c = 3\times10^8$ m/s, $\pi = 3.14$, r is the radius of the slot which is equal to 0.8 mm in the context, and X is the Bessel function whose value is about 3.054 at TM_{21} mode.

$$f(TM_{21}) = \frac{c}{2\pi r}X \tag{1}$$

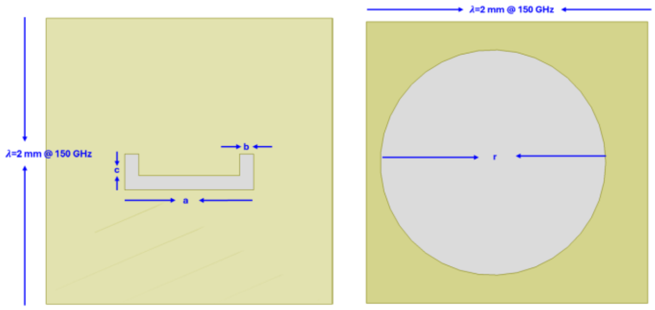

Fig. 1. Proposed dual polarization antenna for sub-THz 6G application: (a) receiver in H-Pol at 180 GHz, (b) transmitter in V-Pol at 150 GHz

Next, to design the Rx antenna at 180 GHz in H-Pol, the ground plane initial length p is about 1.8 mm which is < λ and width q is about 0.1 mm. The substrate design procedure is very similar as Tx substrate design. Though the operating wavelength of 180 GHz is quite smaller than the 150 GHz, for mechanical convince, the substrate dimensions as exactly same as Tx. Then, a rectangular slots length and widths were also same as the substrate design. The thickness of the rectangular patch is 10 um. Then a radiating slot has been designed as shown in Fig. 1(a). This slot will act as radiating element at 180 GHz. Here, the length of the slot is about 0.8 mm which approximately < $\lambda/2$. As per the theory, the half wavelength slot will offer the resonance at fundamental mode that is TE_{10}. However, the operation bandwidth (OBW) at fundamental mode will be too small relatively less than 4 to 5%. Therefore, to supplement or extend the slot apparent length, half wavelength slot has been increased by length "*c*" supplement to initial half wavelength to get higher order mode resonance compared to fundamental resonance mode. The value of the "*c*" is based on the resonance mode of the slot and it has been fixed as 0.25 mm while the antenna operating at TE_{20} mode. To confirm its resonance mode, a detail current distribution analysis has been performed in the next section.

Finally, Figs. 2(a) and 2(b) illustrate the bottom and top views respectively. All physical dimensions of the proposed antenna are listed in Tab. 1.

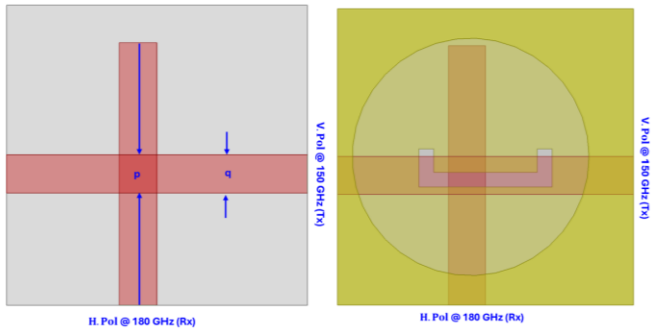

Fig. 2. Proposed dual polarization antenna for sub-THz 6G application: (a) bottom view, (b) top view

Table 1. The list of physical dimensions

Parameter	*a*	*b*	*c*	*q*	*r*	*p*	*q*
Dimension (mm)	0.8	0.1	0.25	0.1	0.4	1.8	2

3 Results and discussions

In the previous section, the Tx and Rx antennas was modelled individually and derived their design concept from the fundamental theory concept. In this section, the Tx and Rx will be combined together as shown in Fig. 3. The proposed antenna configuration consists of a dual-layer, dual-polarized radiating structure designed to support independent transmit (Tx) and receive (Rx) operations in the sub-THz frequency range. As illustrated in Fig. 3, the antenna comprises two stacked radiating elements separated by a dielectric substrate, with each element optimized to operate at a distinct frequency band and polarization state as explained in the previous section. This layered arrangement enables simultaneous Tx/Rx functionality while maintaining a compact footprint suitable for highly integrated 6G front-end modules. The upper radiating layer is dedicated to the transmit path and operates at 150 GHz with vertical polarization (V-Pol). This layer incorporates a circular slot etched in the ground plane, which is specifically engineered to excite the TM_{21} mode. The circular slot geometry promotes azimuthal field variation and polarization purity while suppressing unwanted coupling to the lower layer. The excitation of the TM_{21} mode results in a distinct current distribution that supports vertical polarization and contributes to inherent isolation from the receive antenna.

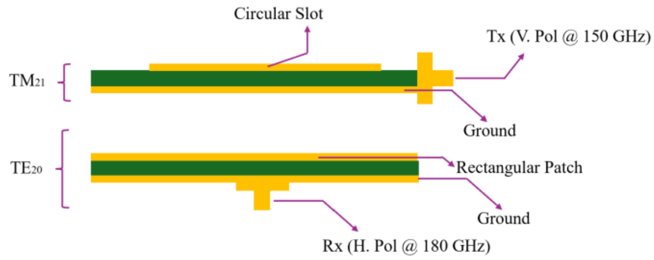

Fig. 3. Proposed dual polarization antennas for sub-THz 6G applications under dual polarization configuration while transmitter and receiver operating at distinct modes

The lower radiating layer functions as the receive element and is designed to operate at 180 GHz with horizontal polarization (H-Pol). This layer employs a rectangular patch radiator backed by a dedicated ground plane and is optimized to excite the TE_{20} mode. The rectangular geometry and feed configuration ensure controlled field distribution along the horizontal axis, enabling orthogonal polarization with respect to the transmit antenna. The use of the TE_{20} mode further enhances modal orthogonality between the Tx and Rx paths. Each radiating element is associated with an independent ground plane, which plays a critical role in suppressing surface-wave coupling and limiting electromagnetic interaction between the two layers. The combination of orthogonal polarizations (V-Pol and H-Pol), distinct operating frequencies, and mode diversity TM_{21} and TE_{20} provides strong intrinsic isolation without the need for additional decoupling structures or lossy isolation components. This self-isolated architecture is particularly advantageous for frequency division duplex (FDD) applications, where simultaneous transmission and reception are required. The proposed dual-polarized antenna structure leverages mode-selective excitation and polarization orthogonality to achieve high Tx-Rx isolation in the sub-THz regime. The design is well suited for 6G transceiver systems, where compactness, low loss, and stable coexistence between transmit and receive channels are essential.

After arranging the Tx and Rx into their respective polarizations, it is very important to know the influence of each variable of the proposed antennas physical parameter. Therefore, a sensitive investigation on each parameter of the proposed antenna has been carried out. This systematic investigation also helps to control and tune the antenna performance. In this study, initially the influence of parameter "*a*" has been investigates. Since the Rx and Tx are very close to each other approximately $< \lambda/2$, therefore the half wavelength slot located at Rx will also influence the performance of the Tx. Therefore, the influence of "*a*" has been investigates for Tx and Rx and investigated simulation results has been shown in Figs. 4(a) and 4(b). The simulated return loss characteristics of the suggested dual-polarized antenna for various rectangular slot length values are shown in Fig. 4. The Tx and Rx ports are examined independently. Figure 4(a) shows the Tx antenna running at about 150 GHz (V-polarization), while Fig. 4(b) shows the Rx antenna operating at approximately 180 GHz (H-polarization). To investigate its impact on impedance matching and resonance behavior, parameter *a* is changed from 0.7 mm to 1.0 mm. Because of the longer slot's increased effective electrical length, raising *a* cause the Tx resonant frequency to shift toward the lower frequency area, as seen in Fig. 4(a). The resonance appears slightly above the target range for *a* = 0.7 mm, but it shifts below the ideal frequency at *a* = 1.0 mm. Around 150 GHz, an ideal value of *a* = 0.8 mm yields the finest impedance matching with a return loss of less than −18 dB. Increasing a likewise causes the resonance to move toward lower frequencies for the Rx antenna, as shown in Fig. 4(b). The rectangular slot has a considerable impact on the modal behavior at 180 GHz, as evidenced by the slightly increased sensitivity of the Rx resonance to *a*. When *a* = 0.8 mm, the resonance achieves excellent impedance matching with return loss less than −20 dB and is in good alignment with the intended Rx band. However, due to significant disruption of the current path, raising a further to 1.0 mm slightly deteriorates the matching. These findings lead to the conclusion that *a* = 0.8 mm is the ideal value for achieving both appropriate resonance placement and adequate impedance matching for the Tx and Rx bands.

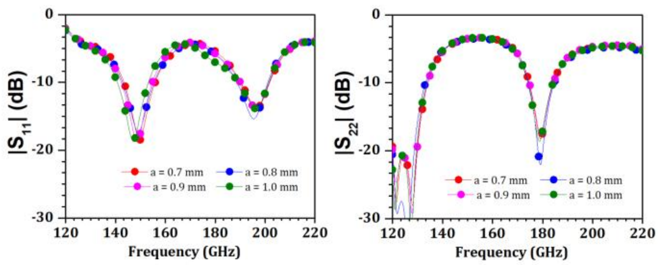

(a) (b)

Fig. 4. The return loss of the (a) transmitter, and (b) receiver under various values of "*a*"

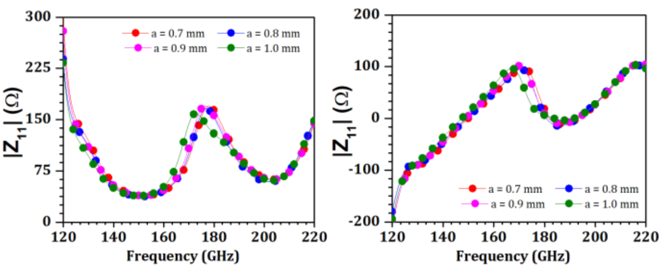

(a) (b)

Fig. 5. The impedance $|Z_{11}|$ of the transmitter at 150 GHz in the V-Pol: (a) real part, and (b) imaginary part under various "*a*"

As seen in Figs. 5(a) and 5(b), the real and imaginary components of the input impedance Z_{11} were examined over the frequency range of 120-220 GHz in order to further investigate the effect of *a*. There are two resonant peaks in the real section of the impedance, both of which move slightly toward lower frequencies as *a* rises. For instance, the peak near 180 GHz for *a* = 0.7 mm shifts to roughly 172 GHz for *a* = 1.0 mm, which is consistent with the structure's increased electrical length. The peak magnitude, on the other hand, stays almost constant, suggesting that a primarily affects the resonant frequency rather than the resistive loss. The resonance condition is confirmed when the imaginary part of the impedance, as depicted in Fig. 5(b), crosses zero close to 150 GHz. The reactance behavior is only slightly impacted by changes in *a*. Furthermore, as is common for resonant antenna configurations, the impedance shows inductive properties above resonance and capacitive characteristics below resonance.

Similarly, Figs. 6(a) and 6(b), which represent the real and imaginary components, respectively, display the Rx impedance characteristics $|Z_{22}|$ for various values of *a*. For all simulated values of *a*, the real part of the impedance is about 50 Ω around 180 GHz, as shown in Fig. 6(a), demonstrating satisfactory impedance matching at the Rx port. In comparison to the other scenarios, the impedance is marginally higher for *a* = 1 mm. For all values of a, a peak impedance of more than 200 Ω around 160 GHz and roughly 150 Ω at 220 GHz is noted. The resonance happens close to 180 GHz, when the reactance passes zero, according to Fig. 6(b). The reactance stays positive over the majority of the simulated frequency range, suggesting inductive-dominant behavior below and above the resonance. Additionally, there is little variance in the reactance curves for various values of a, indicating that the parameter a has little effect on the Rx impedance characteristics.

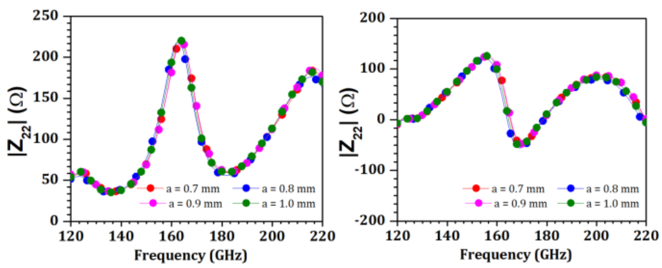

(a) (b)

Fig. 6. The impedance $|Z_{22}|$ of the receiver at 180 GHz in the H-Pol (a) real part, and (b) imaginary part under various "*a*"

The slot width b is the next design parameter taken into consideration after examining the impact of the rectangular slot length a. Figures 7(a) and 7(b) show the simulated return loss of the Tx and Rx antennas for varying values of "b" for V-polarization and H-polarization, respectively. The findings show that better impedance matching is typically achieved with smaller values of b. The return loss at 150 GHz for the Tx antenna improves to around −20 dB when $b = 0.05$ mm. In the upper frequency range (>150 GHz), where greater values marginally deteriorate the impedance matching, the effect of b becomes more apparent. The return loss for the Rx antenna was also assessed in the frequency range of 120-220 GHz. Around 180 GHz, the best matching is found at $b = 0.1$ mm, with a return loss better than −22 dB; the worst matching is found at $b = 0.15$ mm, with roughly −17 dB.

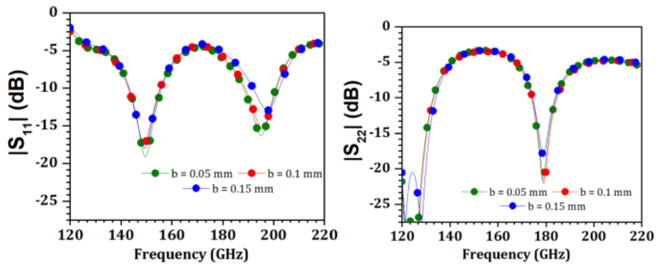

(a) (b)

Fig. 7. The return loss of the (a) transmitter, and (b) receiver under various "b"

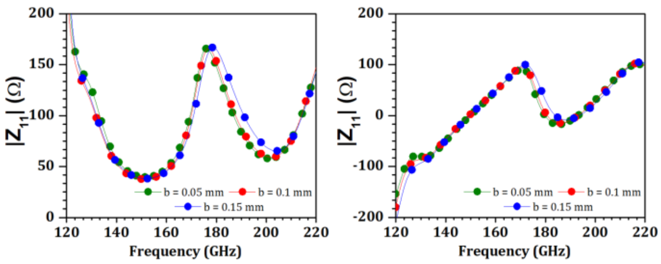

(a) (b)

Fig. 8. The impedance $|Z_{11}|$ of the transmitter at 150 GHz in the V-Pol: (a) real part, and (b) imaginary part under various "b"

Figures 8(a) and 8(b) display the Tx impedance characteristics for various b values. As observed from Fig. 8(a), the real part of the impedance remains close to 50 Ω at 150 GHz, indicating good matching at the resonance frequency. Near 160 GHz, a peak impedance of more than 170 Ω is noted. Higher impedance is produced by smaller values of b in the lower frequency zone (<150 GHz) and bigger values of b in the higher frequency region (>150 GHz). The Tx antenna's reactance behavior is shown in Fig. 8(b). When the reactance crosses zero at 150 GHz, resonance takes place. At the resonance frequency, variations in b result in insignificant changes. As is common with resonant antenna configurations, the antenna behaves capacitively below resonance and inductively above resonance.

The Rx impedance characteristics were investigated similarly, as Figs. 9(a) and 9(b) demonstrate. According to Fig. 9(a), for all values of b, the real part of the impedance stays near 50 Ω at 180 GHz, indicating correct matching at the Rx resonance. For the simulated situations, the maximum impedance exceeds 200 Ω and happens around 162 GHz. The resonance happens at about 180 GHz, according to the reactance characteristics shown in Fig. 9(b). The best response is obtained at this frequency when $b = 0.1$ mm. Both below and above the resonance, the reactance continues to be inductive dominant across the majority of the frequency range.

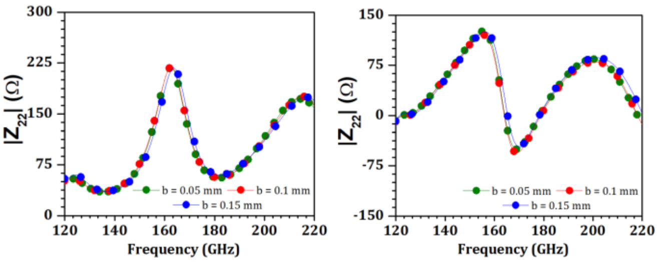

(a) (b)

Fig. 9. The impedance $|Z_{22}|$ of the receiver at 180 GHz in the H-Pol: (a) real part, and (b) imaginary part under various "b"

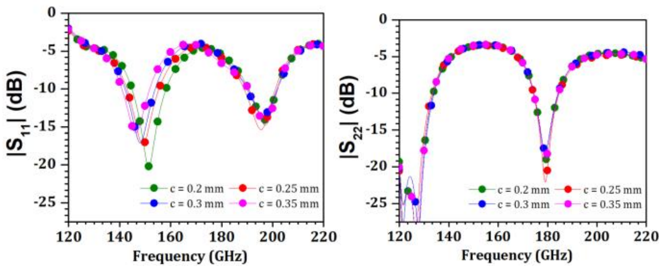

(a) (b)

Fig. 10. The return loss of the (a) transmitter, and (b) Rx under various "c"

Variable c, which adds an extra effective length to the half-wavelength rectangular slot to excite the higher-order TE_{20} mode, was added to the parametric research. Figures 10(a) and 10(b) display the simulated return loss of the Tx and Rx antennas for $c = 0.2$-0.35 mm. Smaller values of c enhance impedance matching for the Tx antenna, with $c = 0.2$ mm achieving a return loss lower than −20 dB close to 150 GHz and $c = 0.35$ mm producing slightly worse performance. On the other hand, the Rx responses are comparatively comparable for all values, with the sharpest notch of about −24 dB at 180 GHz produced by $c = 0.35$ mm. Figures 11(a), 11(b), 12(a) and 12(b) show the comparable impedance characteristics. The true part of the impedance for the Tx antenna peaks at 170 GHz, reaching 150 Ω, and stays close to 50 Ω about 150 GHz. Reactance shows inductive activity above resonance and capacitive behavior close to resonance. The Rx antenna has a maximum impedance of almost 210 Ω around 160 GHz, but the true impedance is likewise close to 50 Ω near 180 GHz. Over the majority of the frequency range, the reactance is primarily inductive and passes zero close to 180 GHz, confirming the resonance.

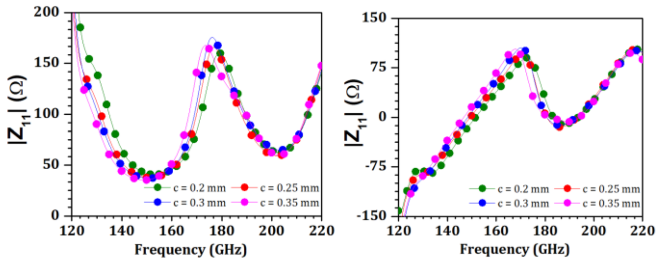

(a) (b)

Fig. 11. The impedance $|Z_{11}|$ of the transmitter at 150 GHz in the V-Pol (a) real part, and (b) imaginary part under various "*c*"

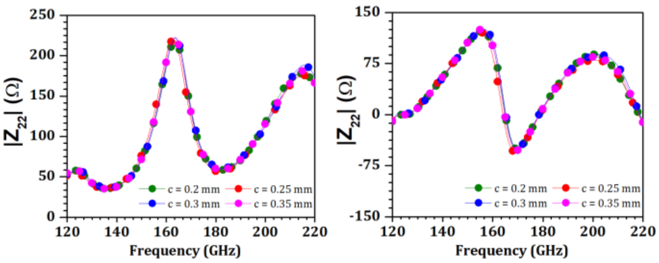

(a) (b)

Fig. 12. The impedance $|Z_{11}|$ of the receiver at 180 GHz in the V-Pol (a) real part, and (b) imaginary part under various "*c*"

The inquiry was expanded to the variable q, which denotes the ground plane width on the bottom layer of the suggested antenna, after parameter c was examined. To investigate its impact on antenna performance, the parameter *q* was changed between 0.1 mm and 0.25 mm.

Figures 13(a) and 13(b) display the corresponding Tx and Rx return loss characteristics. For lower values of *q*, the Tx antenna shows better impedance matching, as shown in Fig. 13(a). Specifically, $q = 0.1$ mm results in a deep return loss notch about 150 GHz, whereas rising *q* causes the resonance to shift toward higher frequencies and somewhat deteriorate the matching. On the other hand, for larger values of *q*, the Rx antenna exhibits improved impedance matching and achieves return loss better than −20 dB, see Fig. 13(b). The Rx resonance is shifted toward higher frequencies by smaller levels of *q*.

Figures 14(a) and 14(b) show the Tx antenna's impedance characteristics. The real part of the impedance stays near 50 Ω at 150 GHz, as shown in Fig. 14(a), demonstrating appropriate impedance matching at the operating frequency. Near 180 GHz, a maximum impedance of more than 250 Ω develops, while $q = 0.3$ mm has the lowest impedance of all the simulated scenarios.

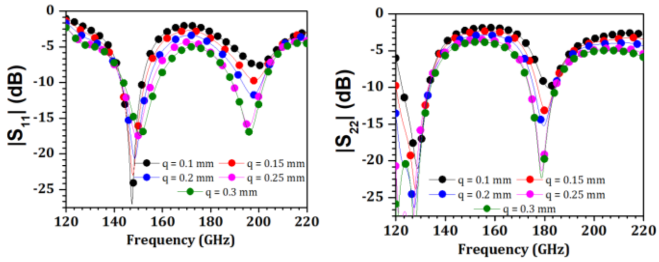

(a) (b)

Fig. 13. The return loss of the (a) transmitter, and (b) receiver under various "*q*"

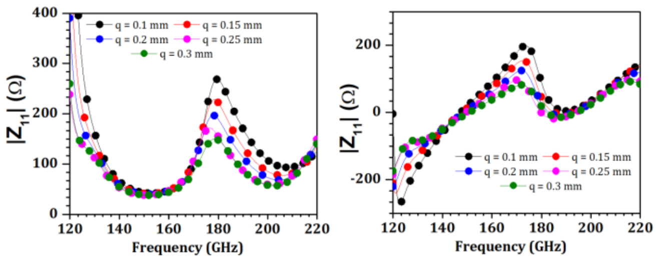

(a) (b)

Fig. 14. The impedance $|Z_{11}|$ of the transmitter at 150 GHz in the V-Pol: (a) real part, and (b) imaginary part under various "*q*"

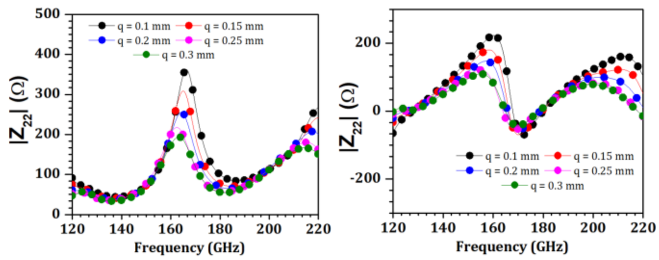

(a) (b)

Fig. 15. The impedance $|Z_{11}|$ of the receiver at 180 GHz in the V-Pol: (a) real part, and (b) imaginary part under various "*c*"

Figures 15(a) and 15(b) display the Rx impedance characteristics for various values of *q*. According to Fig. 15(a), the lowest impedance (less than 200 Ω) happens at $q = 0.3$ mm, whereas the greatest impedance surpasses 340 Ω when $q = 0.1$ mm. For all values of *q*, the resonance condition (zero imaginary part) appears close to 180 GHz, as shown in Fig. 15(b). The Rx impedance shows inductive reactance over the majority of the frequency range, especially for $q = 0.1$ mm. The radius of the circular slot r was the subject of a parametric analysis in order to better optimize the antenna performance.

Figures 16(a) and 16(b) show the return loss responses of the Tx and Rx antennas in the 120-220 GHz frequency range. Excellent impedance matching is demonstrated by the Tx antenna's stable resonance around 150 GHz, where $r = 0.4$ mm results in the deepest return loss surpassing −25 dB. While changes in r mostly impact the lower-frequency region around 125 GHz, the primary resonance for the Rx antenna stays concentrated about 180 GHz. Values of $r = 0.4$-0.6 mm in the target band preserve return loss better than −15 dB.

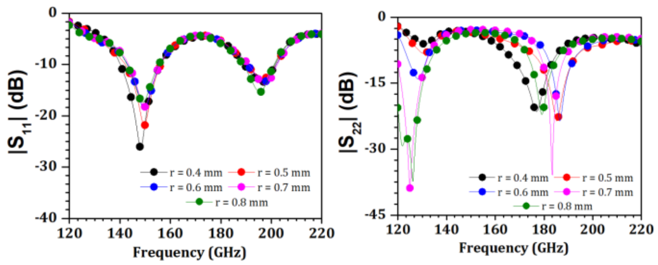

(a) (b)

Fig. 16. The return loss of the transmitter (a) at 150 GHz, and (b) Rx at 180 GHz under various "*r*"

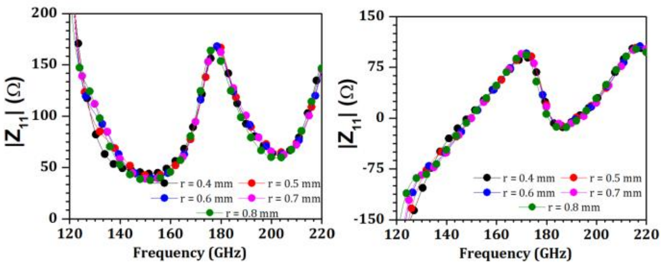

(a) (b)

Fig. 17. The impedance $|Z_{11}|$ of the transmitter at 150 GHz in the V-Pol: (a) real part and (b) imaginary part under various "*r*"

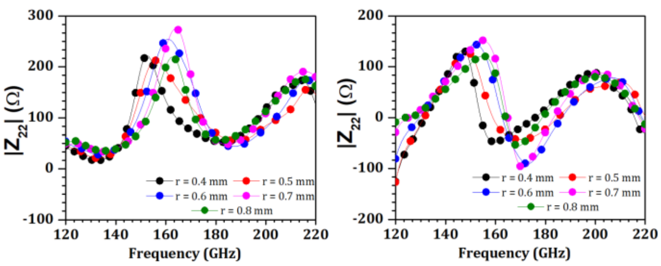

(a) (b)

Fig. 18. The impedance $|Z_{11}|$ of the receiver at 180 GHz in the V-Pol: (a) real part and (b) imaginary part under various "*r*"

Figures 17(a) and 17(b) show the Tx impedance characteristics. For the majority of r values, the actual part of the impedance stays near 50 Ω at 150 GHz, demonstrating stable impedance matching. The resonant behavior is confirmed when the reactance crosses zero around 145-150 GHz. At the design frequency, a smaller radius ($r = 0.4$ mm) results in a reactance that is closer to zero.

Figures 18(a) and 18(b) show the Rx impedance characteristics. The Rx impedance is more sensitive to r than the Tx. The true impedance at 180 GHz ranges from roughly 50 Ω to 100 Ω, with $r = 0.4$ mm offering the closest match to 50 Ω. The resonance point is indicated by the imaginary component crossing zero close to 180 GHz, and changes in r somewhat alter the inductive and capacitive behavior. Overall, the parametric analysis shows that $r = 0.4$ mm offers the optimal trade-off for both Tx and Rx operation, keeping an impedance near 50 Ω with few reactive components and attaining profound return loss at 150 GHz and 180 GHz.

In conclusion, the parametric analysis of the geometrical variables a, b, c, q, and r shows that the suggested dual-polarized antenna exhibits stable modal behavior and controlled resonance tuning. The 150 GHz TM_{21} and 180 GHz TE_{20} resonances exhibit predictable shifts due to the rectangular slot length a, which mainly modifies the effective current route. By altering the capacitive coupling surrounding the aperture, the slot width b affects the impedance matching depth. Higher-order TE_{20} mode excitation in the Rx is made possible by the supplemental length c, guaranteeing adequate bandwidth without interfering with the Tx operation. At the target frequencies, the circular slot radius r controls the modal field distribution and fine-tunes the reactance toward near 50 Ω impedance, while the ground-plane width q influences surface current confinement and modifies matching properties significantly. Crucially, the orthogonal modal excitation between Tx and Rx is maintained despite these parameters shifting resonance positions and matching levels, demonstrating the resilience of the intrinsic self-isolation mechanism across dimensional alterations.

To further validate the radiation mechanism and mode excitation of the proposed design, the surface current distributions for the transmitter and receiver are analyzed at their respective operating frequencies. Figures 19(a) and 19(b) illustrate the current distribution of the Tx at 150 GHz under V-Pol for phases of 0° and 90°. The distribution clearly depicts the excitation of the TM_{21} mode. At phase 0°, the current is predominantly concentrated along the outer edges of the circular radiator, showing strong intensity at the lower-left and top-right quadrants. At phase 90°, the intensity shifts toward the right edge of the structure, maintaining the characteristic nulls and peaks associated with the TM_{21} mode. The current distribution for the Rx at 180 GHz is presented in Figs. 20(a) and 20(b), operating under H-Pol. The antenna excites the TE_{20} mode, which is essential for the receiver's performance at 180 GHz. At phase 0°, strong current concentrations are visible around the U-shaped aperture, particularly at the corners and the feed point, facilitating efficient signal reception. At phase 90°, the current distribution becomes more localized and less intense, with the primary activity concentrated along the bottom edge of the ground plane. Aperture coupling: the distribution demonstrates that the current is effectively coupled around the specific geometry of the Rx, supporting the H-Pol requirement.

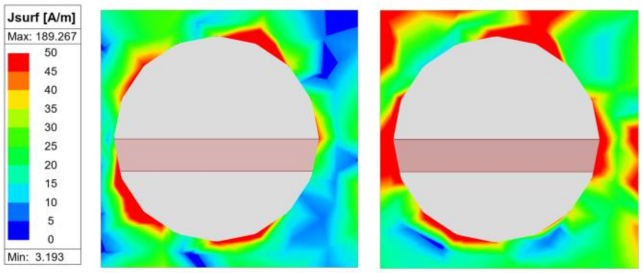

(a) (b)

Fig. 19. Current distribution of the proposed antenna of the transmitter: (a) while phase is 0° degree, and (b) phase is 90° in the V-Pol under TM_{21} mode at 150 GHz

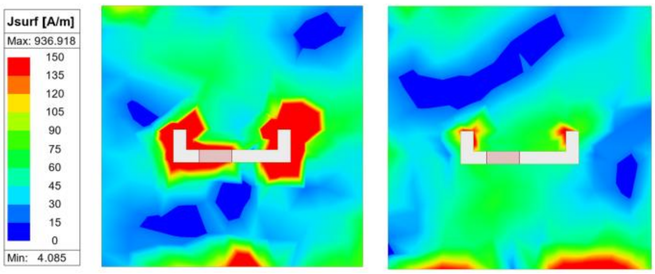

(a) (b)

Fig. 20. Current distribution of the proposed antenna of the receiver: (a) while phase is 0°, and (b) phase is 90° in the H-Pol under TE_{20} at 180 GHz

Their essentially different field configurations and current symmetries are the source of the intrinsic decoupling between the TM_{21} mode of the Tx and the TE20 mode of the Rx. The major vertical electric field components in the TM_{21} mode are aligned with the V-Pol excitation due to the surface current's azimuthal fluctuation with two circumferential maxima and a distinctive nodal distribution. On the other hand, the TE20 mode that is triggered in the Rx enables a field distribution that is primarily horizontal, with negligible vertical field components and two half-wavelength fluctuations along the slot aperture. The spatial overlap integral between the Tx and Rx modal fields becomes intrinsically weak as a result of this orthogonal field orientation and different current symmetry. Additionally, effective power transfer through near-field coupling channels is suppressed because the electric field null regions of one mode physically coincide with the peak regions of the other. Strong intrinsic isolation is thus produced without the need for external decoupling elements since the energy released by the TM_{21} transmitter is ineffective at exciting the TE20 receiving structure. The essential physical process underlying the observed >30 dB Tx-Rx isolation is this modal field orthogonality.

To ensure the accuracy and reliability of the proposed antenna design, comprehensive cross verification was conducted using two independent EM simulation solvers: Ansys HFSS and Altair FEKO. Both HFSS and FEKO solvers were built up with fine mesh parameters and stringent convergence settings to guarantee simulation accuracy at sub-THz frequencies. With a maximum mesh element size of less than λ/30 at the highest simulated frequency (220 GHz) and a con-vergence criterion for S-parameter change of 0.01, an adaptive meshing approach was employed in HFSS. To reduce reflections, radiation boundaries were positioned at least λ/4 from the antenna structure. With fine mesh granularity and enhanced basis function resolution close to slots and edges, the method of moments (MoM) solver was employed in FEKO. In areas of high field fluctuation, manual mesh refinement was used to precisely represent modal behavior. The steady agreement between HFSS and FEKO across criteria for gain, efficiency, isolation, and return loss validates the simulation setup's resilience and lessens the possibility of solver-induced inconsistencies. These safety measures were required because sub-THz simulations are susceptible to numerical artifacts and meshing mistakes. The results demonstrate a high degree of correlation across the targeted frequency bands.

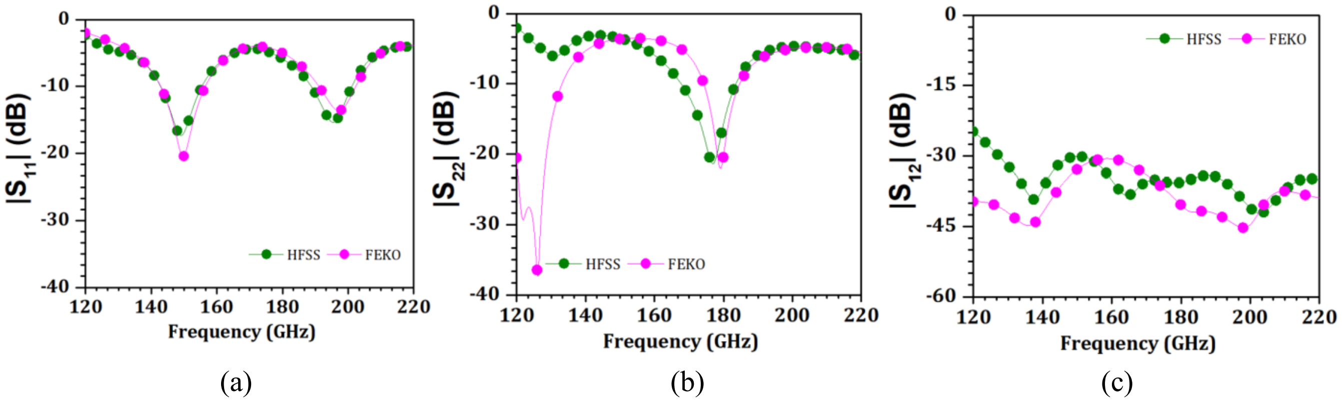

Fig. 21. HFSS and FEKO simulation comparison to verify the correctness of the simulation result: (a) transmitter return loss, (b) receiver return loss, and (c) isolation

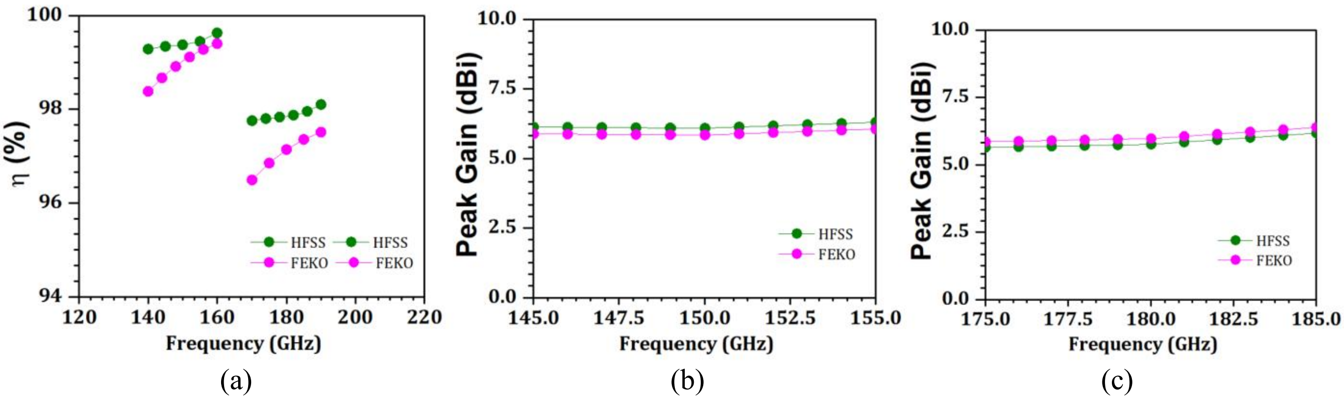

Fig. 22. HFSS and FEKO simulation comparison to verify the correctness of the simulation result: (a) radiation efficiency, (b) transmitter peak gain, and (c) Rx peak gain

Figures 21(a), 21(b) 21(c) provide the comparison of S-parameters between the two software packages. The return loss for the Tx and Rx shows excellent agreement, with both solvers predicting resonances at 150 GHz and 180 GHz respectively. The Tx return loss levels are maintained well below –15 dB at the 150 GHz, while Rx return loss demonstrates a sharp resonance exceeding -20 dB at 180 GHz in both environments. Mutual coupling between the Tx and Rx ports is depicted in Fig. 21(c). The isolation remains significantly better than –30 dB across the entire operating bandwidth. This high isolation is critical for preventing interference between the transmitter and receiver modules in a high-frequency integrated system. The radiation characteristics, including efficiency and peak gain, are summarized in Figs. 22(a), 22(b) and 22(c) respectively. The antenna maintains exceptionally high efficiency, consistently exceeding 96% across both the 150 GHz and 180 GHz bands with maximum radiation efficiency reaches to 99.63%. Minor discrepancies between HFSS and FEKO (within approximately 1%) are observed, which can be attributed to the different numerical methods used for meshing and boundary conditions. As shown in Fig. 23(b), the Tx provides a stable peak gain of approximately 6.0 dBi from 145 to 155 GHz. Similarly, the Rx peak gain, illustrated in Fig. 23(c), remains steady around 6.0 dBi across the 175 to 185 GHz range.

To benchmark the proposed antenna against existing state-of-the-art designs, a comparative analysis is presented in Tab. 2. This comparison evaluates key metrics such as operating frequency, bandwidth, isolation, and efficiency. As summarized in Tab. 1, the proposed design offers several distinct advantages over recently published works: With a compact physical footprint of $2 \times 2 \times 1.508$ mm^3, the antenna is significantly smaller than most designs operating at lower microwave and millimeter-wave frequencies. Operating at a center frequency of 175 GHz, the design achieves a wide isolation bandwidth (IBW) of 51.42%, outperforming many referenced structures that rely on complex decoupling techniques. The proposed antenna reaches a peak radiation efficiency (η) of 99.63%, which is higher than the efficiency reported in [3, 6, 7]. A standout feature of this work is the achievement of 30.12 dB isolation without the need for external decoupling structures like DGS, Cross Stubs, or MCR. This simplifies the fabrication process while maintaining high performance.

Table 2. The performance comparison of the proposed antenna with literature antennas
f = resonance frequency, NA = not accessible, NP = not provided, IBW = isolation bandwidth

Reference	Year	Antenna size	Decoupling technique	f (GHz)	IBW (%)	Isolation (dB)	η(%)	Peak gain (dBi)
[3]	2025	7.6×11×0.51	MCR	28	42.85	25	92.5	4.2
[4]	2025	NA	Graphene metal coating	7420	19.17	30	NP	NP
[5]	2026	52×52×0.8	Cross stubs	32	88	22.5	98.3	10.73
[6]	2025	35×35×0.508	DGS	13	1.5	25	80	7.02
[7]	2025	23×15×1.6	DGS	4	50	28	95	8.3
[8]	2025	16.2×25.6	DGS	7.35	99.31	15	NA	6.2
Proposed	NA	2×2×1.508	No decoupling structure	175	51.42	30.12	99.63	6.44

The far-field radiation characteristics of the proposed antenna are validated through 2D radiation patterns at the primary design frequencies of 150 GHz and 180 GHz. The results from HFSS and FEKO are compared to verify the directional properties of the transmitter (Tx) and receiver (Rx). Figures 23(a) and 23(b) illustrate the radiation patterns for the Tx at 150 GHz under V-Pol, corresponding to the excitation of the TM_{21} mode. The patterns are shown for phi = 0° and phi = 90°. Both simulation solvers predict a relatively broad beamwidth with a peak gain focused towards the boresight direction. There is a high degree of correlation between HFSS (green line) and FEKO (pink line), with only minor deviations observed in the back-lobe regions.

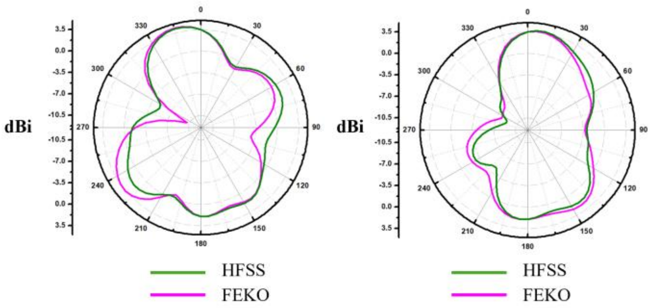

(a) (b)

Fig. 23. The radiation patterns of the proposed antenna of the transmitter (a) while $\phi = 0°$ (E-Plane), and (b) $\phi = 90°$ (H-plane) in the V-Pol under TM_{21} mode at 150 GHz

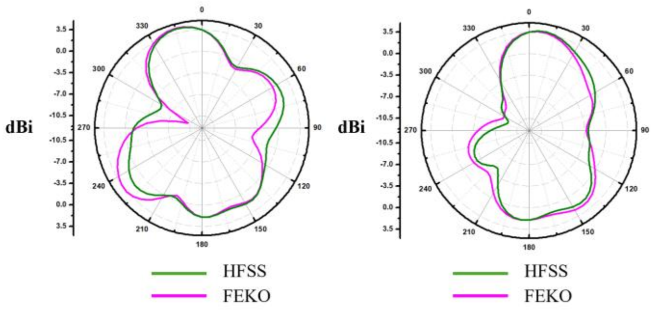

(a) (b)

Fig. 24. The radiation patterns of the proposed antenna of the Rx (a) while $\phi = 0°$ (E-Plane), and (b) $\phi = 90°$ (H-plane) in the H-Pol under TE_{20} mode at 180 GHz

Figures 24(a) and 24(b) present the radiation patterns for the Rx at 180 GHz under H-Pol. The structure for the Rx is designed to operate in the H-Pol state at 180 GHz. The patterns at phi = 0° and phi = 90° exhibit well-defined lobes. The main lobe intensity remains consistent across solvers, confirming stable directive gain at the higher frequency band.

It is crucial to recognize the practical difficulties related to fabrication and experimental validation at sub-THz frequencies, even if the current study is fully simulation-based [16]. Because even micrometer-level variations in patch geometry, feed-line width, or ground-plane dimensions can drastically alter the resonant frequency and impair impedance matching and isolation performance, dimensional tolerances become crucial at these frequencies. Additionally, differences between simulated and measured findings may be caused by substrate parameter uncertainties, specifically variances in the dielectric constant and loss tangent at sub-THz bands [17, 18]. Conductor losses, which are frequently underestimated in full-wave simulations, are further increased by the metallization layer's surface roughness. From the measurement standpoint, precise characterization necessitates sub-THz compliant connectors, high-precision probe stations, and meticulous calibration methods like TRL (Thru-Reflection Line) or SOLT (Slot-Open Load Thru) to reduce systematic errors. Notwithstanding these practical difficulties, the simulated results offer a solid theoretical basis for upcoming fabrication and experimental validation.

To understand the effect of antenna element separation on mutual coupling, a parametric study was conducted by varying the gap between the Tx and Rx antennas from 0.5 mm to 2 mm, which approximately corresponds to λ/4 to λ within the operating frequency range. The simulated transmission coefficient S_{12} for different separations is shown in Fig. 25.

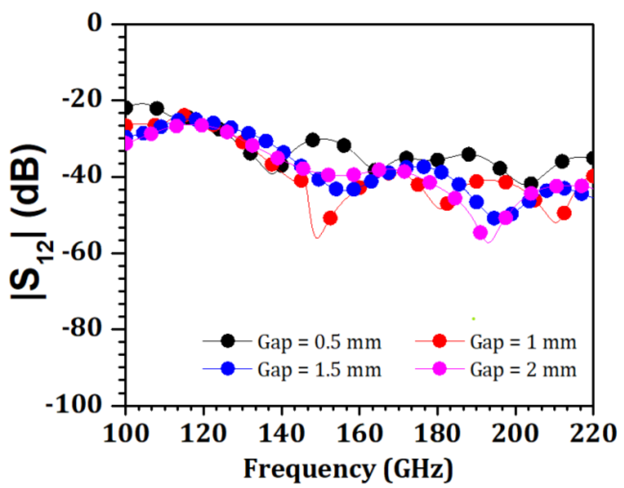

Fig. 25. The proposed antenna's isolation as a function of gap separation between the transmitter and receiver

The results indicate that increasing the separation generally reduces mutual coupling, as the electromagnetic near-field interaction between the two radiating elements decreases. For the smallest gap (0.5 mm), the antennas exhibit relatively higher coupling because strong reactive near-field components exist between the closely spaced elements. As the spacing increases to 1 to 1.5 mm, the isolation improves significantly, remaining below approximately −35 dB across most of the operating band. When the separation approaches 2 mm (≈λ), the isolation is further improved in several frequency regions, reaching values below −50 dB. However, the variation with frequency is not strictly monotonic due to frequency-dependent field coupling, surface-wave propagation on the substrate, and phase interactions between the radiated fields. These results confirm that the selected spacing provides a suitable trade-off between compact antenna integration and high isolation performance.

To further evaluate the proposed antenna design, simulation results were cross-verified using two full-wave electromagnetic solvers, FEKO and HFSS, as shown in Fig. 26. The comparison includes critical MIMO performance characteristics such as Envelope Correlation Coefficient (ECC), Diversity Gain (DG), and Channel Capacity Loss (CCL) at operating frequencies ranging from 120 to 220 GHz. As illustrated in Fig. 25(a), the ECC values obtained from both solvers are extremely similar and remain very low across the whole band, declining from around 0.018 at 120 GHz to virtually nil at higher frequencies up to 220 GHz, indicating very little correlation between the antenna ports. Effective diversity performance is confirmed by Fig. 25(b), which demonstrates that the DG stays nearly constant at about 10 dB across the working region. Additionally, throughout the whole frequency range, the CCL values shown in Fig. 25(c) stay below 0.3 bits/s/Hz, meeting the widely recognized MIMO performance requirements. The consistency and dependability of the simulated performance of the suggested antenna construction are demonstrated by the strong agreement between the FEKO and HFSS results.

Future research will use circuit-based simulation tools like Keysight Advanced Design System (ADS) to create an equivalent circuit model of the suggested antenna. From a circuit-level perspective, the RLC-based representation will offer more insight into the antenna's impedance behavior and resonance characteristics. The full-wave electromagnetic validation carried out with ANSYS HFSS and Altair FEKO will be significantly enhanced by this investigation.

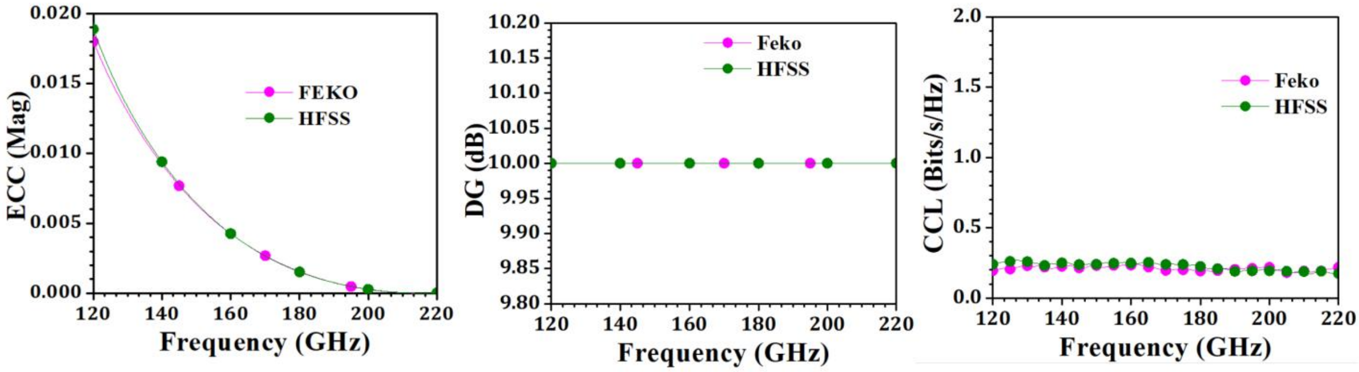

(a) (b) (c)

Fig. 26. HFSS and FEKO simulation comparison to verify the correctness of the simulation result: (a) ECC, (b) DG, and (c) CCL

4 Conclusion

This paper describes a self-isolated dual-polarized patch antenna for sub-THz 6G transceiver applications that achieves strong Tx-Rx isolation without the usage of any additional decoupling structures. The suggested method takes advantage of intrinsic electromagnetic properties by purposely stimulating orthogonal higher-order modes in the transmit and receive channels. The transmitter operates in the TM_{21} mode with vertical polarization at 150 GHz, while the receiver excites the TE_{20} mode with horizontal polarization at 180 GHz. When combined with an orthogonal feeding setup, this mode-selective excitation produces little field overlap and significantly reduced mutual coupling at the antenna level. The impact of important geometrical parameters on impedance matching, resonance stability, and modal behavior has been thoroughly investigated using extensive parametric analyses. The results show that fine control over slot size and ground-plane parameters allows for separate tuning of the Tx and Rx resonances while maintaining polarization purity and modal orthogonality. Surface current distribution study reveals satisfactory excitation of the targeted $TM_{21}$and TE_{20} modes, verifying the isolation mechanism physically. The suggested antenna achieves an isolation level more than 30 dB over a wide isolation bandwidth of 51.42% ranging from 130 GHz to 220 GHz, which is especially important for frequency division duplex (FDD) operation in the sub-THz range. Despite its small size ($2\times2\times1.508$ mm³), the antenna achieves a peak radiation efficiency of 99.63% and a consistent peak gain of 6.44 dBi. Cross-verification with the HFSS and FEKO solvers shows significant agreement in S-parameters, radiation efficiency, gain, and radiation patterns, verifying the proposed design's resilience and numerical dependability. A thorough comparison with previously published antennas reveals that many present methods use defective ground structures, parasitic elements, or material-based decoupling strategies to improve isolation, typically at the sacrifice of bandwidth, efficiency, or structural simplicity. In contrast, the suggested antenna achieves competitive or higher isolation and efficiency without requiring extra decoupling devices, simplifying fabrication and boosting scalability for highly integrated sub-THz front-end modules. Overall, this study shows that mode-based self-isolation, accomplished by higher-order mode excitation and polarization orthogonality, is an effective and realistic method for reducing Tx-Rx coupling in tiny sub-THz antennas. The suggested design is ideal for future 6G transceiver systems that require strong isolation, wide bandwidth, and great radiation efficiency in a compact form factor. Future research could broaden this notion to include experimental validation, array-level integration, and on-chip or package-integrated implementations to better serve upcoming sub-THz wireless communication platforms.

References

[1] "From mmWave to THz: Antenna challenges in 6G networks," Available online: https://medium.com/@minakshmi16/from-mmwave-to-thz-antenna-challenges-in-6g-networks-b3bfdcd68a8a.

[2] S. Dash and A. Patnaik, "Material selection for THz antennas," *Microwave and Optical Technology Letters*, vol. 59, no. 6, pp. 1360–1364, 2017.

[3] A. Salem, H. Djellab, M. Lashab, O. Allaoua, M. Elwanis, C. H. See and R. Abd-Alhameed, "High isolation and high gain of MIMO antennas with FSS for 5G mm-wave applications," *Microwave and Optical Technology Letters*, vol. 68, 2025.

[4] H. Yadav, R. Yadav, Y. Goswami, M. Rai and A. Kumar, "Dielectric resonator-based tunable circularly polarized THz MIMO antenna with split ring resonator for isolation control method," *Journal of Optics*, vol. 28, 2025.

[5] T. Addepalli, V. Thota, M. V. Sudhakar, J. C. Rao, C. Swamy, S. Medasani, P. Badugu and A. Al-Gburi, "A novel isolation-enhanced four-element high-gain hexa-band MIMO antenna for 5G mmWave systems," *Wireless Personal Communications*, pp. 1–21, 2026.

[6] B. Rezaee, A. Abdi, S. Javadi and W. Bösch, "Compact four-port Ku-band MIMO antenna with enhanced isolation using modified DGS for early-phase 6G applications," *Electronics*, vol. 15, p. 94, 2025.
[7] R. Manikonda, A. Sudhakar and G. Tamminaina, "Isolation enhancement of four-port multiple-input multiple-output antenna for sub-6 GHz 5G communication," *Bulletin of Electrical Engineering and Informatics*, vol. 14, pp. 4433–4442, 2025.
[8] D. Rajendran, S. Ramesh, D. Kumar and O. Kumar, "Compact octagonal MIMO antenna system for broadband applications with enhanced isolation and wideband performance," *Scientific Reports*, vol. 15, 2025.
[9] W. Fuscaldo, F. Maita, L. Maiolo, R. Beccherelli and D. C. Zografopoulos, "Broadband dielectric characterization of high-permittivity Rogers substrates via terahertz time-domain spectroscopy in reflection mode," *Applied Sciences*, vol. 12, no. 16, p. 8259, 2022.
[10] A. Bhutani, J. Dittmer, L. Valenziano and T. Zwick, "Sub-THz conformal lens integrated WR3.4 antenna for high-gain beam-steering," *IEEE Open Journal of Antennas and Propagation*, vol. 5, no. 5, pp. 1306–1319, 2024.
[11] C. J. Park, D. Jung, J. Seo, T. S. Kwon, B. Ahn and S.-H. Wi, "Isolation improvement technique in dual-polarized antenna for sub-THz antenna-in-package," *IEEE Antennas and Wireless Propagation Letters*, vol. 22, no. 12, pp. 3032–3036, 2023.
[12] Y. Lyu, Z. Yuan, M. Li, A. W. Mbugua, P. Kyösti and W. Fan, "Enabling long-range large-scale channel sounding at sub-THz bands: Virtual array and radio-over-fiber concepts," *IEEE Communications Magazine*, vol. 62, no. 2, pp. 16–22, 2024.
[13] P. Zhang, P. Kyösti, K. Haneda, P. Koivumäki, Y. Lyu and W. Fan, "Out-of-band information aided mmWave/THz beam search: A spatial channel similarity perspective," *IEEE Communications Magazine*, vol. 62, no. 2, pp. 86–92, 2024.
[14] M. Khalily, O. Yurduseven, T. J. Cui, Y. Hao and G. V. Eleftheriades, "Engineered electromagnetic metasurfaces in wireless communications: Applications, research frontiers and future directions," *IEEE Communications Magazine*, vol. 60, no. 10, pp. 88–94, 2022.
[15] Z. Chen *et al*., "Terahertz wireless communications for 2030 and beyond: A cutting-edge frontier," *IEEE Communications Magazine*, vol. 59, no. 11, pp. 66–72, 2021.
[16] A. Hussain and T. Hussain, "AI-Driven Resource Allocation and Beamforming in 6G Terahertz Networks," International Journal of Communication Systems39, no. 7, 2026.
[17] G. S Uthayakumar, N. Praveena, K. Manikandan, and Purnimakadali Sharma, "Smart MIMO Antennas with Spatio-Temporal Graph Neural Networks for Advanced 6G and IoT Communication" *Journal of Circuits, Systems and Computers*, 10.1142/S0218126626501811.
[18] Wurood Fadhil Abbas, Muhammad N. Jawad, Hamzah Hadi Qasim, and Ahmed Hameed Majeed, "6G-Enabled IOT: Emerging Communication Technologies, AI Integration, and Future Research Directions" *Asian Journal of Research in Comupter Science,* Vol. 19, pp. 173 – 191, 2026.

S. Bhoopalan currently works as Assistant Professor in ECE Department of Muthayammal Engineering College, Rasipuram. He received his B.E. degree in Electronics and Communication Engineering from Muthayammal Engineering College, Anna University in 2010 and M.E. degree in Communication Systems from Rajalakshmi Engineering College, Anna University in 2012. Currently pursuing PhD in the area of Microwave antennas. His current research includes microstrip antennas, microwave applications, orthogonal frequency division multiplexing (OFDM), embedded systems and their application to wireless communication

U. Saravanakumar is Professor and Head of the Department of Electronics and Communication Engineering at Muthayammal Engineering College, Rasipuram. He has held the position since 2019. He previously served at Vel Tech University, PSG College of Technology, and Sri Ramakrishna Engineering College. He obtained Bachelor of Engineering in ECE, Master of Engineering in VLSI Design and PhD in Information and Communication Engineering from Anna University. His research interests include VLSI Design and Antenna Engineering.

J. Kirubakaran has worked as Associate Professor in ECE Department, Muthayammal Engineering College, Rasipuram, since 2018. He received his B.E., (ECE) and M.E. (Communication Systems) in 2005 and 2010 respectively. He completed his PhD (Information and Communication Engineering) in 2017 in Anna University, Chennai.

R. Muddineni works for Foxconn in Taiwan as a Senior Radio Frequency R&D Engineer. He graduated with a Bachelor of Technology in Electronics and Communication Engineering from Vel Tech University in Chennai, India, and a Master of Science in Passive Circuits Design from National Ilan University in Taiwan in 2022. RF passive circuit design, including antennas, filters, diplexers, and power dividers, is one of his areas of interest. His work has mostly focused on using the ideas of genetic optimization algorithms to improve the comprehension, design, and performance of broadband antennas.

Received 22 January 2026